Ceramics International 46 (2020) 950–958

Contents lists available at ScienceDirect

Ceramics International

journal homepage: www.elsevier.com/locate/ceramint

Enhanced electrical and thermal conductivities of 3D-SiC(rGO, G*x*) PDCs based on polycarbosilane-vinyltriethoxysilane-graphene oxide (PCS-VTES-GO) precursor containing graphene fillers

Yuchen Han[a,b,c], Lei Zhong[a,b,c], Yinong Zheng[a,b,c], Rui Zhou[a,b,c], Liang Liao[a,b,c], Guolong Chen[d], Wenyan Huang[a,b], Shuyu Lin[a,b], Yuejin Zhong[a,b], Junbin Li[a,b], Wei Zheng[a], Rongqian Yao[a,b,c,*]

[a] Department of Materials Science and Engineering, College of Materials, Xiamen University, Xiamen, 361005, China
[b] Fujian Key Laboratory of Advanced Materials (Xiamen University), Xiamen, 361005, China
[c] Key Laboratory of High Performance Ceramics Fibers (Xiamen University), Ministry of Education, Xiamen 361005, China
[d] Fujian Engineering Research Center for Solid-state Lighting, Department of Electronic Science, Xiamen University, Xiamen, 361005, China

ARTICLE INFO

Keywords:
SiC
Polycarbosilane
Graphene
Electrical conductivity
Polymer-derived ceramics

ABSTRACT

Lightweight 3D-SiC(rGO, G*x*) PDCs were fabricated from polycarbosilane-vinyltriethoxysilane-graphene oxide (PCS-VTES-GO) precursor added by different amounts of graphene fillers via direct cold molding and pyrolysis at 1400 °C in an easy manner. Results reveal that SiC(rGO, G*x*) PDCs consist of β-SiC nanocrystals homogeneously embedded within amorphous SiO*x*C*y*/C_{free}, and graphene is well compatible with SiO*x*C*y*/C_{free} for void-free bonded interface, efficiently delaying decomposition of SiO*x*C*y* phase into β-SiC. The nanocomposite structure provides an ingenious strategy for constructing complexes with good integrity, high ceramic yield, excellent thermal stability, high electrical and thermal conductivities. This improvement is primarily attributed to the presence of graphene with considerably increasing electric-charge carriers and wider phonon-channel. Such 3D-SiC(rGO, $G_{20\%}$) PDCs possess satisfying hardness (12.02 GPa), high electrical conductivity (23.82 S cm^{-1}) and thermal conductivity (7.47 W m^{-1} K^{-1}), which make them attractive candidates for microelectromechanical systems (MEMS) devices, energy storage/conversion systems and high precision components, etc.

1. Introduction

In recent years, materials with lightweight, improved mechanical strength at elevated temperatures, excellent corrosion resistance and chemical stability attract much attention for their utilization on aerospace, petrochemical and nuclear systems [1–3]. Among them, silicon carbide (SiC) polymer-derived ceramics (PDCs) are promising for above fields owing to their intrinsic advantages such as low density, low thermal expansion coefficient, high elastic modulus, high hardness, good thermal shock resistance and reasonable permittivity [4]. These prominent features endow them with potential applications in high precision components, microelectromechanical systems (MEMS) and future fusion reactors, etc [5–7]. SiC PDCs realize a significant breakthrough in low-dimensional forms including fibers, coatings, films, micro-patterns or membranes [8–12]. Despite this, their popularity is limited by fabrication techniques of three-dimensional (3D) samples [13].

3D-SiC PDCs are being examined for potential electrochemical energy storage and micro-systems applications, owing to free carbon network and hybrid bonds of Si with O and C atoms as well as improved complex and near-net-shape forming capability. Among others with the integration of outstanding mechanical strength and functional features make them excellent candidates for many interesting and emerging technology programs [14,15]. Several efforts have been successfully devoted to preparing 3D-SiC as structural-functional materials from liquid precursors (shaping using molding, warm-pressing or 3D-printing technique) [16–18]. Furthermore, many attempts have been made to improve process and even final material properties via adding fillers or modifying solid precursors [7,19,20]. However, less explored are electrical and thermal properties of 3D-SiC PDCs which also open up new potential applications such as high temperature sensors, MEMS devices, electrodes materials for Li-ion batteries, conductive protective coatings and supercapacitors, etc [21–25].

Partial replacement of O by C in SiO*x*C*y* mixed phase and presence of free carbon network embedded inside amorphous matrix from 3D-SiC PDCs can increase their electrical conductivity [26]. In addition to

* Corresponding author. Department of Materials Science and Engineering, College of Materials, Xiamen University, Xiamen, 361005, China.
E-mail address: rqyao@xmu.edu.cn (R. Yao).

https://doi.org/10.1016/j.ceramint.2019.09.056
Received 3 August 2019; Received in revised form 4 September 2019; Accepted 5 September 2019
Available online 06 September 2019

this, there are many important parameters used to modify electrical response such as pyrolysis temperature, introduction of conductive fillers, and precursor compositions like type or amount of carbon [25,27,28]. Simultaneously, addition of a high thermal conductivity filler into the matrix can also contribute to improving thermal conductivity, but this requires high temperature stability of fillers during pyrolysis. Furthermore, retaining high compactness of PDCs matrix after filler introduction for compensating the drawback of SiO*x*C*y* in poor electrical conductivity and thermal conductivity is still challenging. Gratifyingly, graphene has attracted much attention as filler to enhance the above material properties. Growth of graphene on the single-crystal SiC by thermal decomposition has revealed that graphene might be well compatible with SiC [29]. Thus, adding graphene into 3D-SiC PDCs is expected to realize the integration of high densification, high electrical conductivity and high thermal conductivity.

In our previous work, novel 3D-SiC(rGO) monoliths with good compactness, high hardness and low linear shrinkage were successfully fabricated with polycarbosilane-vinyltriethoxysilane-graphene oxide (PCS-VTES-GO) precursor. Their microstructure consists of β-SiC nanocrystals, amorphous SiO*x*C*y*, rGO and free carbon. As a graft composite and sintering additive, GO can enlarge the cross-linking structure, promote the molding ability, inhibit the growth of SiC nanocrystal, and reduce the pyrolysis temperature. However, much higher C contents are needed when 3D-SiC(rGO, G*x*) PDCs are to be used as an electrically and thermally conductive material.

As a result of the motivation, this study is further to insert graphene fillers to PCS-VTES-GO precursors for fabricating fully dense, crack-free and carbon-rich 3D-SiC(rGO, G*x*) PDCs. The main emphasis is on the microstructural and structural characterization of the 3D-SiC(rGO, G*x*) PDCs with the objective of understanding their thermal stability, electrical conductivity and thermal conductivity properties as a function of the amount of graphene addition. After that, 3D-SiC(rGO, $G_{20\%}$) PDCs were applied as heat dissipation substrates for high-power LED devices and further as special conductors in circuit to verify their thermal stability and electrical conductivity at high temperature in air. It provides the first study and exciting new data on the tunable electrical and thermal transport of these carbon-rich 3D-SiC PDCs which need to operate in harsh environments at elevated temperature.

2. Experimental section

2.1. Preparation of 3D-SiC(rGO, Gx) PDCs

Polycarbosilane (PCS) employed in this research were synthesized in our laboratory, Graphene and GO were acquired from TANFENG graphene Tech Co., Ltd. (Suzhou, China), Karstedt catalyzer was provided by Dong Sheng Synthetic Material Co., Ltd. (Dongguan, China), VTES was supplied by Diamond Chem Co., Ltd. (Nanjing, China), hydrochloric acid and xylene were purchased from Sinopharm Chemical Reagent Co., Ltd. (Shanghai, China).

Schematic diagram of preparing 3D-SiC(rGO, G*x*) PDCs and images of monoliths before and after pyrolysis are illustrated in Fig. 1. First, PCS powders (1 g) were dissolved in xylene (20 mL) and then GO powders (0.01 g) were mixed into deionized water (20 mL). After that, the above two solutions were dispersed through an ultrasonic bath for 30 min. Subsequently, Karstedt catalyzer (0.05 mL) was added into the solution of PCS/xylene. Then VTES (1 mL) was added into GO/water solution and dilute hydrochloric acid (5 wt%) was used to adjust the pH of GO/VTES/water solution to 1–2. Afterward, the above-mentioned PCS/xylene/Karstedt solution and GO/VTES solution were mixed together. The mixed layered solution was heated to 60 °C and maintained for 1 h in water-bath. After standing for 5 min, a biphasic mixture was formed. The upper gray layer was the product while the transparent bottom layer was water, then the upper layer was put into a rotary evaporator in vacuum and distilled at 70 °C. The obtained solids were finally milled into fine PCS-VTES-GO powder products. These PCS-VTES-GO powder products with different weights of graphene (0 wt%, 5 wt%, 10 wt%, 15 wt% and 20 wt%) were mixed with ethanol. The slurry was milled and dried to remove the solvent and obtain a uniform mixture then pressed in a steel mold with a diameter of 17 mm under 82 MPa. The green compacts were pyrolyzed in Ar (flow rate: 200 mL min^{-1}) at a heating rate of 5 °C min^{-1} to 1400 °C and maintained for 30 min to obtain 3D-SiC(rGO, G*x*) PDCs. In addition, PIP (precursor infiltration and pyrolysis) route was applied to further densify SiC(rGO, $G_{20\%}$) PDCs. The sample was infiltrated in liquid PCS for 24 h followed by pyrolyzing at 1000 °C in Ar and repeated 5 cycles to obtain final SiC(rGO, $G_{20\%}$) PDCs.

2.2. Analysis and characterization

3D-SiC(rGO, G*x*) PDCs with different graphene contents were characterized by the following ways. The bulk density was measured using the Archimedes' method and porosity was calculated employing both bulk and real density values following:

$$P(\%) = (1 - Bulk\ density/Real\ density) \times 100 \quad (1)$$

The linear shrinkage was determined by the following formula:

$$shrinkage\ (\%) = \left(\frac{d_0 - d}{d_0}\right) \times 100 \quad (2)$$

where d_0 was the diameter of PCS-VTES-GO/Graphene compacts and d was the diameter of 3D-SiC(rGO, G*x*) PDCs. Surface morphology of the samples was observed using a scanning electron microscope (SEM, Model 1530, LEO, Germany). Their composition and microstructure were investigated by electron probe microanalysis (EPMA, JXA-8100, JEOL, Japan), Fourier transform infrared spectrometer (FTIR, Nicolet Avatar FTIR 360, USA), X-ray diffractometer (XRD, AxsD8, Bruker, Germany), Raman spectrometer (IDSpec ARCTIC, China) and transmission electron microscope (TEM, Tecnai F30, Philips-FEI, USA). Electron-paramagnetic-resonance (EPR) measurements were performed on an EPR spectrometer (ER 200D-SRC, Bruker, USA) using X-band to determine the charge state of defects and impurities. The Vickers hardness of the samples was tested by Microhardness Instrument (TMVS-1, Beijing Time High Technology, China) using a 0.98 N load. Calculation of fracture toughness (K_{IC}) was based on the following equation:

$$K_{IC} = 0.016 \times \left(\frac{E}{H}\right)^{0.5} \times \frac{P}{c^{1.5}} \quad (3)$$

where 0.016 is a constant, E is Young's modulus (Gpa), H is hardness (Gpa), P is the indentation load (2.94 N in this test), and c is half length of the crack. The room temperature electrical conductivity (σ) of samples was measured using four-point probes resistivity tester (RTS-9, Guangzhou Four-probe electronic technology, China) in accordance with ASTM F1529-97. Thermal gravimetric analysis (TGA, SDT Q600, NETZSCH STA, Germany) was used to determine the weight loss during heat treatment (25 °C-1400 °C) with a heating rate of 10 °C·min^{-1} in flowing Ar. Thermal diffusivity measurements were performed at 25 °C by a laser-flash apparatus (LFA 467, NETZSCH, Germany). Thermal conductivity (κ) was calculated using the following equation:

$$\kappa = \alpha \cdot \rho \cdot C_p \quad (4)$$

where α is the thermal diffusivity, ρ is the density of the specimen, C_p is the specific heat.

Afterward, to verify their heat dissipation ability, 3D-SiC(rGO, G*x*) PDCs were further used as heat dissipation substrates for representative high-power LED devices via chip-on-board (COB) package. Firstly, silver paste (GW-02, UV TECH, China) was used to bond high-power LED chips (APT4040B, APT Electronics, China) onto substrate and baked at 150 °C for 1.5 h. Subsequently, electrodes of the chips were connected to Cu electrodes through bonding gold wires by a wire bonder (WT-2310, Baixiangyuan, China). Phosphor silicone was

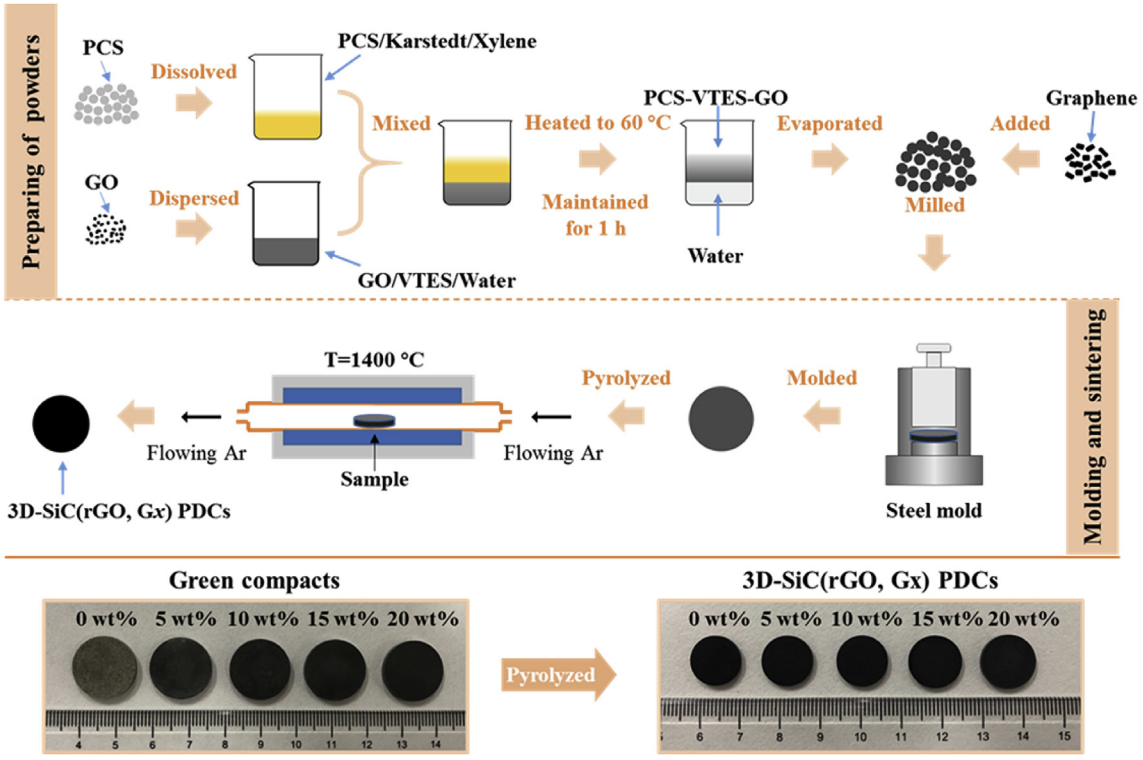

Fig. 1. Schematic diagram of preparing 3D-SiC(rGO, G*x*) PDCs and images of monoliths before and after pyrolysis.

dispersed on the surface of chips and bonding gold wires to form a phosphor layer and then baked at 120 °C for 1 h. Thermal resistance and junction temperature (the temperature of active region in LED devices, this important parameter influences their performances, such as efficiency, output power, reliability, peak wavelength shift, and spectral width) of the high-power LED devices based on 3D-SiC(rGO, G*x*) PDCs were tested and calculated in a transient thermal tester (T3ster, MicReD Ltd., Hungary). Furthermore, such SiC (rGO, $G_{20\%}$) was chosen to connect with LED devices through an electric circuit to test their thermal stability and electrical conductivity at high temperature in air.

3. Results and discussion

Table 1 shows physical properties and elemental compositions of 3D-SiC(rGO, G*x*) PDCs. The bulk density decreases from 2.06 g cm^{-3} to 1.75 g cm^{-3} as graphene content increases gradually to 20 wt% which resulted from the addition of lightweight graphene phase. As expected, ceramic yield increases whereas linear shrinkage decreases with rising graphene amounts, owing to the presence of graphene which possesses excellent thermal stability in Ar and even partly hinders the decomposition of SiO*x*C*y* into β-SiC, amorphous free carbon, gaseous SiO and CO during pyrolysis process. Particularly, the decline of gaseous SiO also enhances their ceramic yield. Open porosity of 3D-SiC(rGO, G*x*) PDCs increases from 9.8% to 16.3% owing to graphene softer phase with a fairly large amount of 3D constrained network, which is in favor of thermal stress relaxation during pyrolysis. Based on EPMA results, Si and O contents (the O content mainly comes from VTES) decrease whereas C content increases from 32.11 wt% to 43.23 wt% with increasing graphene addition in the starting precursor, which is conducive to improving electrical and thermal conductivities of 3D-SiC(rGO, G*x*) PDCs.

Fig. 2 exhibits FTIR spectra of 3D-SiC(rGO, G*x*) PDCs with different amounts of graphene (peaks at 1080 cm^{-1} and 780 cm^{-1} due to Si–O–Si stretching vibration and Si–C stretching vibration, respectively), intensity of Si–O–Si is gradually enhanced while that of Si–C is reduced with increasing graphene content. Moreover, the increasing characteristic peak intensity ratios of 1080 cm^{-1} to 780 cm^{-1} for the samples reveal that graphene can effectively postpone the decomposition of SiO*x*C*y* phase into β-SiC during pyrolysis process [25]. Interestingly, the quantity of Si–O–Si bonds increase whereas O content decreases from EPMA, which is corresponding to more magnitude of the rise in graphene content.

Fig. 3(a) depicts XRD patterns of 3D-SiC(rGO, G*x*) PDCs pyrolyzed at 1400 °C. The characteristic peak at 2θ = 26.48° is corresponding to (002) plane of multilayered graphene, and its intensity increases with increasing amounts of graphene addition. There are three main broad peaks at 35.878°, 61.318° and 71.671° ascribed to (111), (220) and (311) planes of crystalline β-SiC respectively [13]. By using Scherrer

Table 1
Physical properties and elemental composition of 3D-SiC(rGO, G*x*) PDCs.

Sample	Bulk density (g·cm^{-3})	Ceramic yield (%)	Linelar shrinkage (%)	Open Porosity (%)	Elemental composition (wt%)			Empirical formula
					Si	C	O	
SiC(rGO, $G_{0\%}$)	2.06	80.78	25.92	9.8	54.39	32.11	13.49	$SiC_{1.38}O_{0.44}$
SiC(rGO, $G_{5\%}$)	2.03	82.56	25.13	10.3	52.66	34.31	13.03	$SiC_{1.52}O_{0.43}$
SiC(rGO, $G_{10\%}$)	1.96	84.64	24.19	11.3	49.90	37.52	12.58	$SiC_{1.75}O_{0.44}$
SiC(rGO, $G_{15\%}$)	1.88	86.22	23.06	12.5	46.80	41.62	11.58	$SiC_{2.07}O_{0.43}$
SiC(rGO, $G_{20\%}$)	1.75	88.84	22.13	16.3	45.67	43.23	11.09	$SiC_{2.21}O_{0.42}$

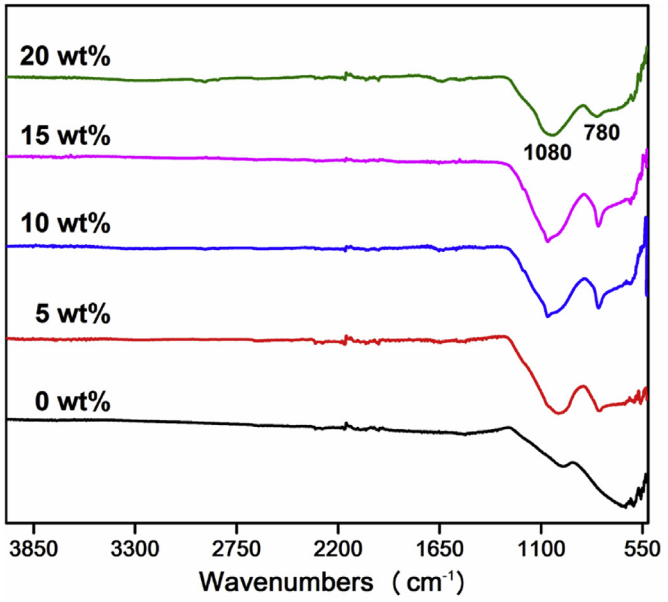

Fig. 2. FTIR spectra of 3D-SiC(rGO, G*x*) PDCs.

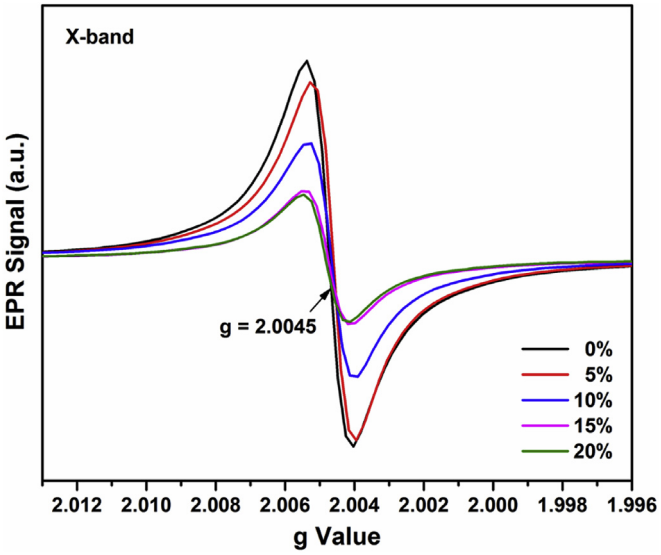

Fig. 4. EPR spectra of 3D-SiC(rGO, G*x*) PDCs.

equation from half-value width of (111) peak (2.14, 2.49, 2.62, 2.70 and 2.87 corresponding to 0 wt%, 5 wt%, 10 wt%, 15 wt% and 20 wt% graphene addition), average crystallite sizes of β-SiC grains in 3D-SiC(rGO, G*x*) PDCs are calculated to be 3.9 nm, 3.4 nm, 3.2 nm, 3.1 nm and 2.9 nm. These results demonstrate that the specific localization of graphene may impede the β-SiC grain boundary migration and partly limit the grain growth during pyrolysis process. Raman spectroscopy is an effective and non-destructive method for characterization of carbon-containing materials. As shown in Fig. 3(b), the D-band at 1335 cm^{-1} corresponds to disordered carbon or defects and the G-band at 1600 cm^{-1} is related to the in-phase bond-stretching of all pairs of sp^2 atoms in rings and chains. Other peaks like 2D-band (at 2650 cm^{-1}) owing to π band of graphitic electronic structure and the D + G band (at 2920 cm^{-1}) attributed to two-phonon process involving D and G phonons are also available [30]. Actually, G-band and 2D-band are the main characteristics of graphite or graphene carbon materials, whereas D-band and D + G band are related to structural defects in the carbonaceous materials. The intensity ratio of I_D/I_G is used to assess the defect level of graphene. The I_D/I_G ratio of SiC(rGO, G*x*) PDCs with 0%, 5%, 10%, 15% and 20% graphene content is corresponding to 0.97, 1.15, 1.37, 1.19 and 1.52 respectively, revealing that more structural and chemical short-range disorders and microcrystalline defects present in samples with higher amounts of graphene [31].

EPR is an effective method to investigate unpaired electrons of 3D-SiC(rGO, G*x*) PDCs in more detail. In Fig. 4, an isotropic signal centered at g = 2.0045, which is the signal for Si-dangling bonds formed during pyrolysis owing to the release of hydrogen and methane in the SiO*x*C*y* phase [32]. All symmetric resonance lines possess common features and similar electronic properties, suggesting defect centers are uniformly distributed and amorphous phases are isotropy. Moreover, the intensity of EPR spectrum decreases with the rise of graphene content, indicating a reduction of defect concentration related to Si-dangling bonds generated from decomposition of SiO*x*C*y*. Since the graphene can effectively delay the decomposition, more graphene addition leads to the decrease of Si-dangling bond amounts. Additionally, possible mechanism to explain this defect concentration reduction is the transformation of the Si-dangling bonds into Si–C bonds [33].

TGA was performed to understand thermal stability of 3D-SiC(rGO,

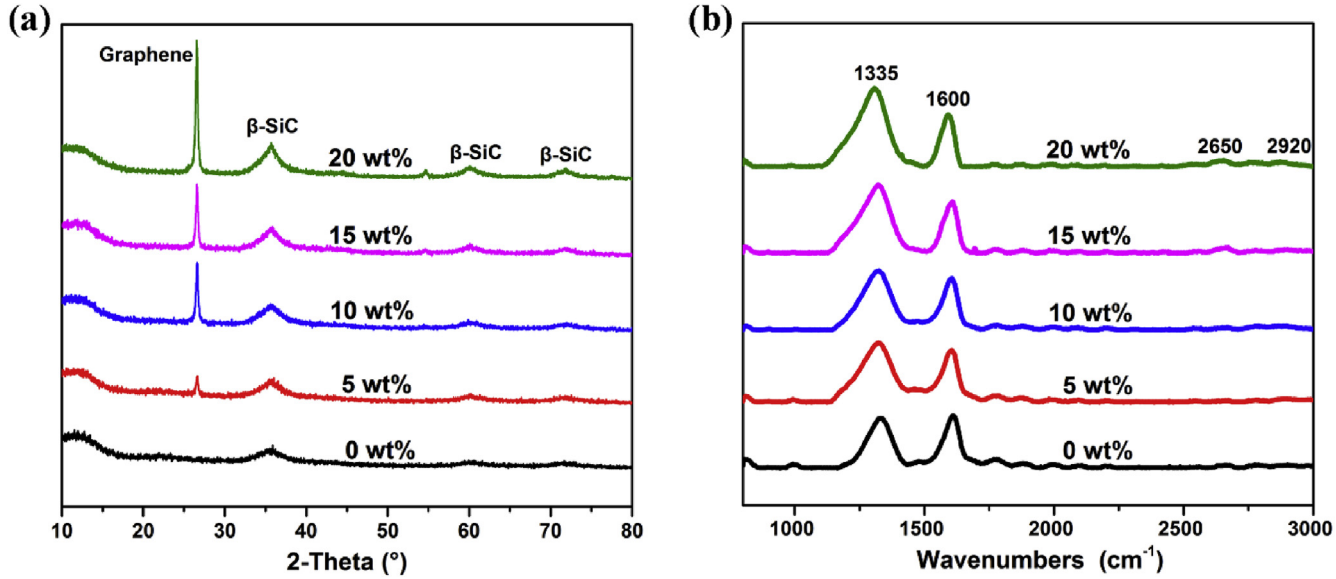

Fig. 3. (a) XRD and (b) Raman spectra of 3D-SiC(rGO, G*x*) PDCs.

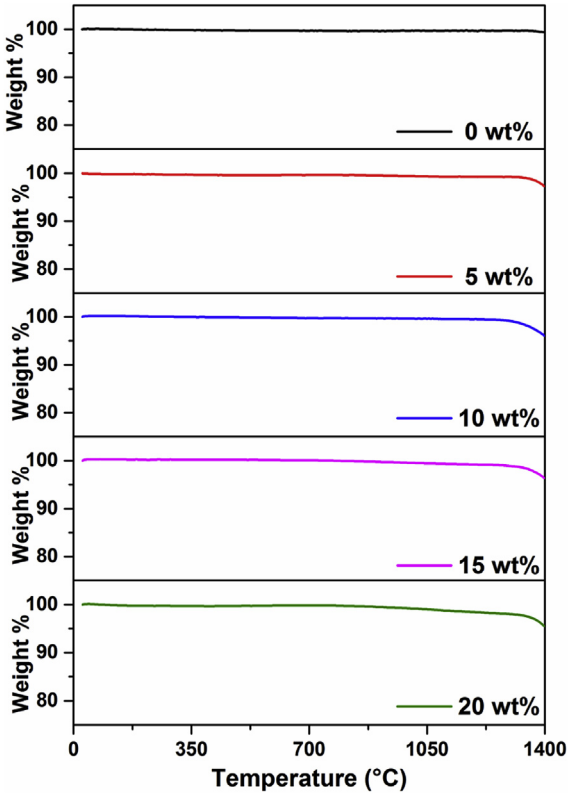

Fig. 5. TGA curves of 3D-SiC(rGO, G*x*) PDCs.

G*x*) PDCs. In Fig. 5, TGA curves exhibit no notable weight loss from room temperature to 1000 °C. Moreover, the weight loss at 1400 °C is 0.56%, 3.12%, 3.43%, 3.67% and 4.12% corresponding to 0 wt%, 5 wt %, 10 wt%, 15 wt% and 20 wt% graphene addition respectively. The observations reveal that 3D-SiC(rGO, G*x*) PDCs own an excellent thermal stability, and thus they are reliable for potential applications in harsh environments.

In Fig. 6(a), hardness of 3D-SiC(rGO, G*x*) PDCs slightly decreases with rising graphene addition. Graphene hinders the conversion of amorphous SiO*x*C*y* phase into nanocrystalline β-SiC, which has a negative impact on hardness. Furthermore, nanostructure of multiple graphene layers results in reduction of hardness in β-SiC/SiO*x*C*y*/C_{free}. These two factors, as well as the rise of graphene addition, lead to the downward tendency of hardness. Fig. 6(b) shows the influence of graphene content on K_{IC} of 3D-SiC(rGO, G*x*) PDCs. The values of the samples are lower than that of SiC(rGO) without graphene addition and decrease with increasing graphene amounts addition. This reduction is related to the intrinsic lower K_{IC} value of multilayered graphene softer phase [34]. Although 3D-SiC(rGO, $G_{20\%}$) PDCs own the lowest hardness and fracture toughness of all, they could still be adequately considered for many potential applications.

Fig. 7(a) illustrates electrical conductivity values for SiC(rGO, G*x*) PDCs at room temperature. As expected, the values of these SiC(rGO, G*x*) PDCs undergoes a huge increase from 1.09×10^{-2} S cm^{-1} to 23.82 S cm^{-1} as graphene content increases gradually to 20 wt%. Since free carbon and crystalline SiC can only offer relatively limited electrical conductivity, the significant rise can be attributed to the introduction of graphene networks. The evolution of thermal conductivity values for SiC(rGO, G*x*) PDCs with different graphene contents is shown in Fig. 7(b). It is noteworthy that the value increases up to 7.47 W m^{-1} K^{-1} with the addition of 20 wt% of graphene, which indicates the great effect of graphene with free-moving electric-charge carriers in the thermal conductivity of carbon-enriched β-SiC/SiOC composites.

Fig. 8 shows the representative SEM micrographs of simply polished surfaces of 3D-SiC(rGO, G*x*) PDCs. Here it is observed that all surfaces appear dense but generate some pores (as well as the higher magnification of insets). Formation of these pores also leads to development of micro cracks on the surface, which has a certain influence on the material mechanical properties. As graphene addition increases, more pores can be seen randomly distributed on the surfaces. With regards to further densify SiC(rGO, $G_{20\%}$) PDCs and reduce their defects, PIP process was applied [16]. As expected, micro-pores on the surface is much less and smaller through the comparison between Fig. 8(e) and (f) and the porosity decreased from 16.3% to 0.04% after repeated PIP process for 5 cycles.

To investigate microstructure of SiC(rGO, $G_{20\%}$) PDCs with high electrical and thermal conductivities in more detail, TEM analysis was performed and the results are demonstrated in Fig. 9. It clearly indicates that β-SiC nanocrystals are homogeneously embedded within amorphous SiO*x*C*y*/C_{free} after high temperature heat treatment, as shown in Fig. 9(e) [13]. In addition, the random close-packed SiO*x*C*y* is close to complete crystal and exhibits a synergistic effect in the thermal conductivity enhancement of 3D-SiC(rGO, G*x*) PDCs. Fig. 9(c) displays the thick stacking nanostructure of multiple graphene layers. The graphene and SiO*x*C*y* phase are well-bonded without gaps and voids at the interface, suggesting graphene might be well compatible with SiO*x*C*y*. As

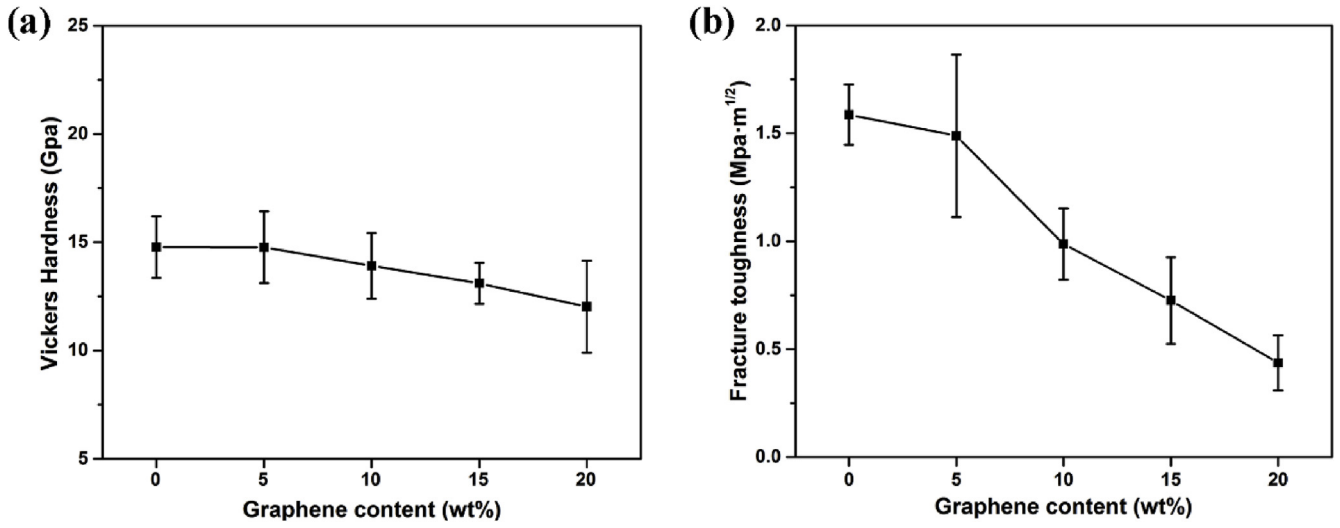

Fig. 6. (a) Hardness and (b) fracture toughness of 3D-SiC(rGO, G*x*) PDCs.

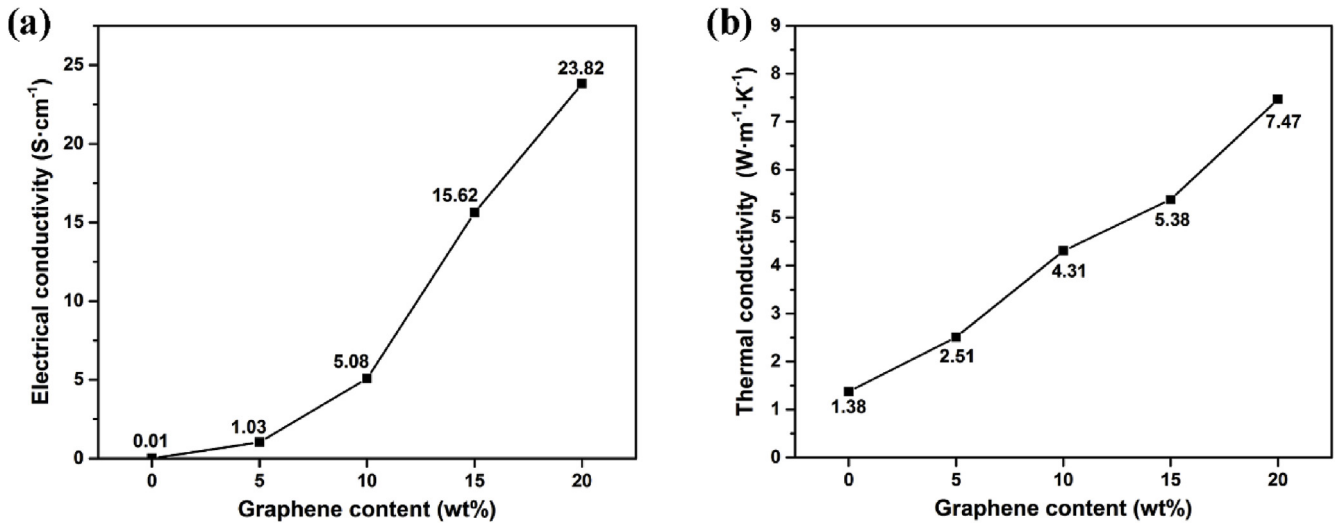

Fig. 7. (a) Electrical and (b) thermal conductivities of 3D-SiC(rGO, G*x*) PDCs.

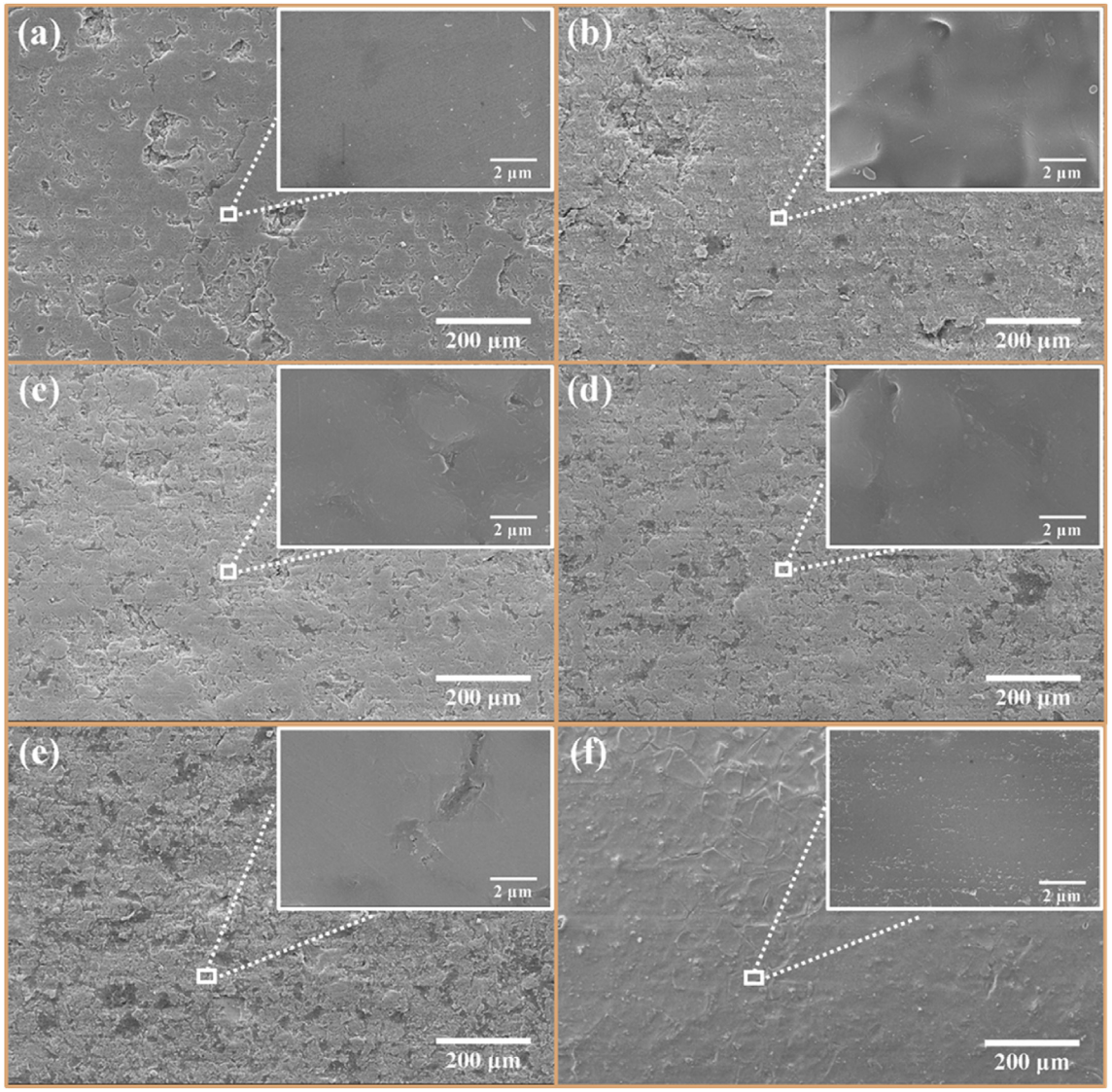

Fig. 8. SEM images of 3D-SiC(rGO, G*x*) PDCs (a) 0 wt%, (b) 5 wt%, (c) 10 wt%, (d) 15 wt%, (e) 20 wt% and (f) 20 wt% via PIP route for 5 cycles.

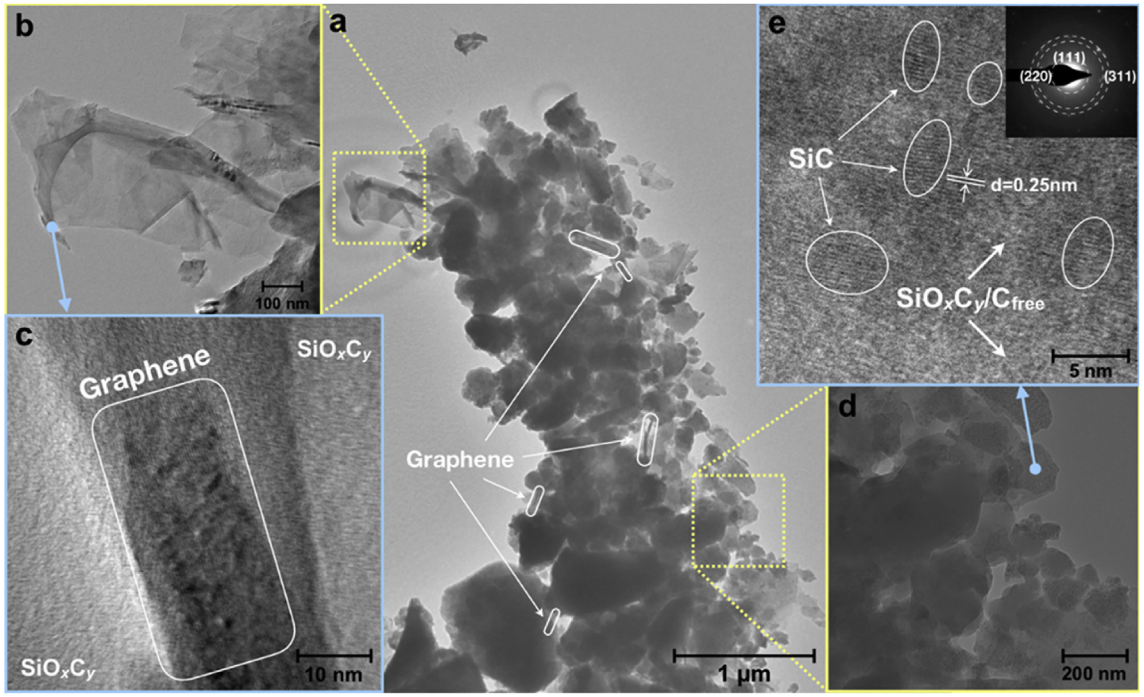

Fig. 9. (a) TEM images of 3D-SiC(rGO, G*x*) PDCs; (b) and (d) Magnification of TEM images of 3D-SiC(rGO, G*x*) PDCs; (c) and (e) HRTEM images of β-SiC and amorphous SiO*x*C*y*/C_{free}.

electron diffraction (SAED) pattern shown, three broad rings corresponding to the (111), (220), (311) planes of β-SiC phase [35]. Fig. 9(e) shows 0.25 nm interplanar spacing assigned to (111) plane of β-SiC. The SiO*x*C*y* phase would decompose into β-SiC, free carbon, SiO and CO above 1000 °C [36]. However, the presence of higher graphene content can efficiently hinder the separation of SiO*x*C*y* phase and crystallization of β-SiC during pyrolysis, which may enhance oxidation resistance of SiC(rGO, G*x*) PDCs at elevated temperature [25].

To verify their heat dissipation ability, 3D-SiC(rGO, G*x*) PDCs were applied as heat dissipation substrates for high-power LED devices to test thermal resistances and junction temperatures of LED devices (see Supplementary Materials for more details) [37]. As shown in Fig. 10(a), 3D-SiC(rGO, G*x*) PDCs evidently affect thermal dissipation of LED devices, both of thermal resistances and junction temperatures decrease significantly with increasing graphene addition, suggesting graphene networks provide a quicker and more effective heat transmission. Moreover, LED device based on 3D-SiC(rGO, $G_{20\%}$) owns a junction temperature of 41.55 °C, which is much lower than the upper limit of 120 °C for common LEDs [38,39]. Interestingly, 3D-SiC(rGO, $G_{20\%}$) with excellent electrical conductivity was chosen to connect with LED devices through an electric circuit to test their electrical conductivity at high temperature (about 1300 °C) in air. As shown in Fig. 10(b) and the video (see Supplementary Materials), it is worth noting that the 3D-SiC(rGO, $G_{20\%}$) PDCs keep stable under butane gun flame and remain high electrical conductivity to link circuit lighting up blue LED device with an output of 3.2 V. Fig. 10(c) shows XRD pattern of 3D-SiC(rGO, $G_{20\%}$) PDCs after the test of butane gun flame. It is noteworthy that the characteristic peak at 2θ = 21.942° is corresponding to α-cristobalite. Additionally, the diffraction peak at 2θ = 26.48° ascribed to (002) plane of multilayered graphene and three peaks assigned to (111) (2θ = 35.878°), (220) (2θ = 61.318°) and (311) (2θ = 71.671°) planes of β-SiC phase are also available. Elemental analysis on the surface of the resultant samples was performed by EPMA. As expected, Si, O and C contents are 47.17 wt%, 45.99 wt% and 6.84 wt% respectively, the atomic ratio of Si to O is close to 1:2, suggesting that SiO_2 can be generated on the surface of 3D-SiC(rGO, $G_{20\%}$) by passive oxidation under butane gun flame in air. To further investigate their surface morphology, SEM measurement was carried out and the images are shown in Fig. 10(d). It is illustrated that dense SiO_2 passivation layer is formed on the surface as evidenced by the uniform surface without observed cracks and pores, reducing diffusion rate of air and preventing the PDCs from further oxidation. Furthermore, electrical conductivity of 3D-SiC(rGO, $G_{20\%}$) PDCs after the test of butane gun flame, which was directly measured by four-point probes resistivity tester, is 2.26×10^{-5} S cm^{-1} owing to the formation of SiO_2 layer on their surface. Based on the results in Fig. 10 (b) and the video, the sample in electrical circuit can still light up blue LED device as a special conductor under high temperature flame, which infers that electrical conductivity is mainly contributed by most of the unoxidized part in 3D-SiC(rGO, $G_{20\%}$) PDCs and relatively unaffected by insulating SiO_2 layer. Thus, the resultant samples were polished to remove SiO_2 layer and their electrical conductivity was re-examined. As expected, the value of the polished 3D-SiC(rGO, $G_{20\%}$) is 25.00 S cm^{-1}, which is slightly higher than that of untreated samples owing to the high temperature flame partly promoting the decomposition of SiO*x*C*y* phase into more free carbon.

Generally, SiOC PDCs possess low electrical conductivity ($< 10^{-3}$ S cm^{-1}) [40], whereas the formation of free carbon and crystalline SiC can only increase electrical conductivity to 1.09×10^{-2} S cm^{-1} for 3D-SiC(rGO) PDCs. According to the above experimental investigations on electrical and thermal conductivities, it is worth mentioning that electrical conductivity of 3D-SiC(rGO, $G_{20\%}$) increases up to three orders of magnitude compared with 3D-SiC(rGO) without graphene addition, which must be corresponding to graphene networks in the 3D-SiC(rGO, G*x*) PDCs. Free-moving electrical-charge carriers in the carbon-enriched β-SiC/SiOC frameworks increase remarkably owing to the increasing amounts of graphene with high electron mobility. Simultaneously, the considerably increasing electric-charge carriers in the samples are significantly conducive to improving their thermal conductivity.

For 3D-SiC(rGO), heat conduction by phonons mostly transfer via only one equivalent phonon-channel. Since the width of equivalent phonon-channel is fixed, their heat conduction is limited as well. However, as graphene content increases, a new equivalent phonon-channel for heat conduction could be assumed to appear owing to the

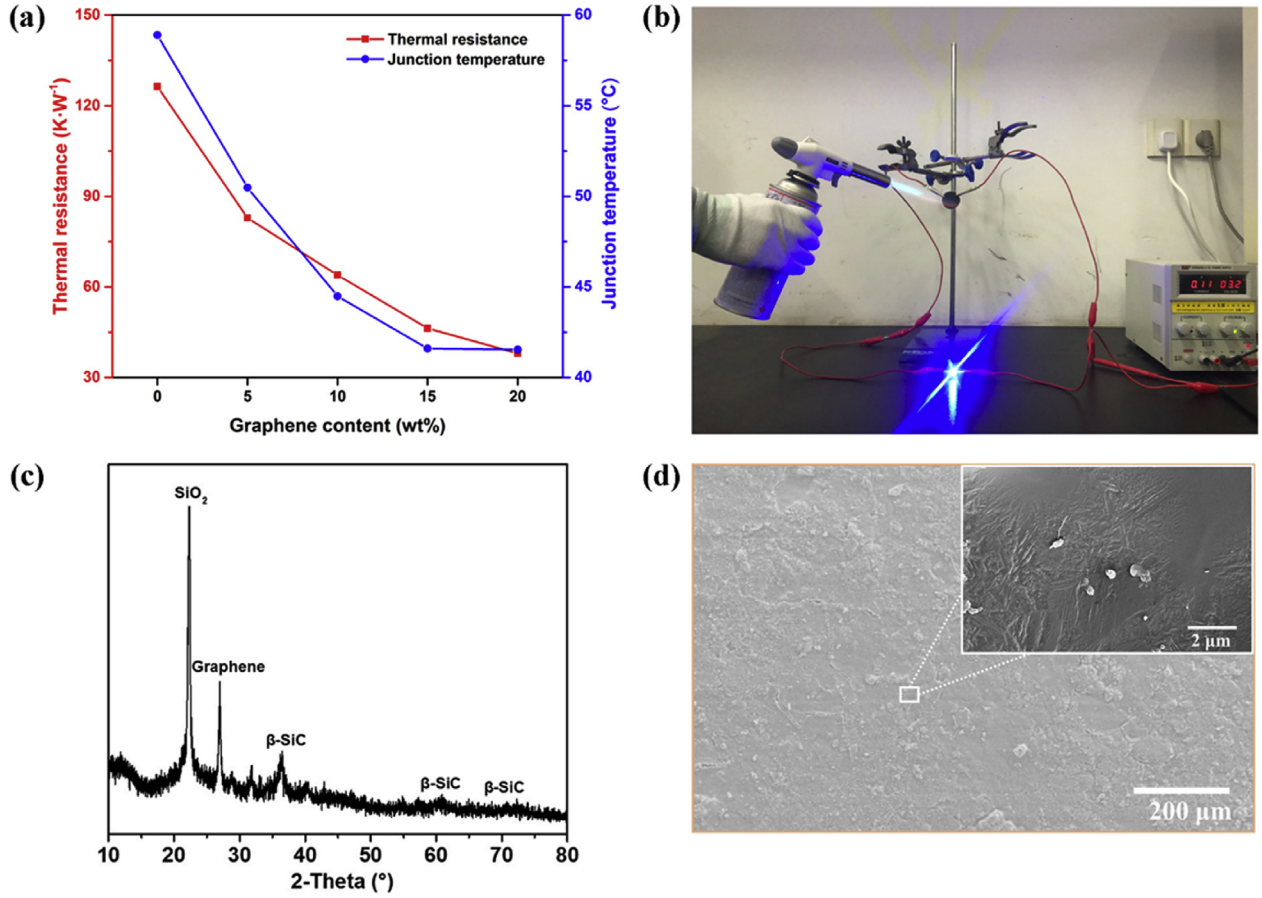

Fig. 10. (a) Thermal resistance and junction temperature of LED devices based on 3D-SiC(rGO, G*x*) PDCs substrates. (b) 3D-SiC(rGO, $G_{20\%}$) in electrical circuit as a special conductor under high temperature flame at 1300 °C can still light up blue LED device based on 3D-SiC(rGO, G*x*) as heat dissipation substrate. (c) XRD spectra and (d) Surface SEM images of 3D-SiC(rGO, $G_{20\%}$) PDCs after the test of butane gun flame. (For interpretation of the references to colour in this figure legend, the reader is referred to the Web version of this article.)

intrinsic high thermal conductivity of graphene in 3D-SiC(rGO, G*x*) PDCs. Thus, 3D-SiC(rGO, G*x*) samples demonstrate a higher thermal conductivity attributed to more electric-charge carriers and wider phonon-channel. Nevertheless, many important factors still need to be evaluated in the future. For example, investigations of their surface oxidation behavior at high oxygen partial pressure and elevated temperature are of interest. Moreover, their fracture toughness can be further improved by controlling type and content of inert fillers. Such 3D-SiC(rGO, G*x*) PDCs with satisfying structural and functional features are expected to be widely applied in the field of aerospace, MEMS and even high precision components.

4. Conclusion

In this paper, fully dense, crack-free and carbon-rich 3D-SiC(rGO, G*x*) PDCs were successfully prepared by inserting graphene fillers to PCS-VTES-GO precursors. This study demonstrates that graphene with wider phonon-channel and more electric-charge carriers can effectively promote the electrical and thermal conductivities and even improve the ceramic yield of 3D-SiC PDCs. Besides, hardness is scarcely influenced, whereas fracture toughness of 3D-SiC(rGO, G*x*) PDCs is certainly affected by graphene soft phase but still maintains at a relatively high level. Their microstructure consists of β-SiC nanocrystals homogeneously embedded within amorphous SiO_xC_y/C_{free}, and graphene is well compatible with SiO_xC_y/C_{free} based on void-free bonded interface. High graphene content can efficiently delay separation of SiO_xC_y phase, which is vital for oxidation resistance of SiC(rGO, G*x*) PDCs at elevated temperatures. Particularly, the resultant 3D-SiC(rGO, $G_{20\%}$) PDCs with high electrical conductivity (23.82 S cm^{-1}) and thermal conductivity (7.47 W m^{-1} K^{-1}), offer new potential emerging uses as high precision components, high temperature sensors and MEMS devices, conductive protective coatings and electrochemical energy storage.

Acknowledgements

This work was supported by the National Natural Science Foundation of China (Grant No. 51302237), the Science and Technology Program of Fujian Province (Grant No. 2016H6021) and the XMU Training Program of Innovation and Enterpreneurship for Undergraduates (Grant Nos. 201810384004, 2018X0642 and S201910384299).

Appendix A. Supplementary data

Supplementary data to this article can be found online at https://doi.org/10.1016/j.ceramint.2019.09.056.

References

[1] C. Ferraro, E.G. Tuñon, V.G. Rocha, S. Barg, M.D. Fariñas, G. Sernicola, F. Giuliani, E. Saiz, Light and strong SiC networks, Adv. Funct. Mater. 26 (2016) 1636–1645 https://doi.org/10.1002/adfm.201504051.
[2] L. Jin, K. Zhang, T. Xu, T. Zeng, S. Cheng, The fabrication and mechanical properties of SiC/SiC composites prepared by SLS combined with PIP, Ceram. Int. 44 (2018) 20992–20999 https://doi.org/10.1016/j.ceramint.2018.08.134.
[3] M. Li, X. Zhou, H. Yang, S. Du, Q. Huang, The critical issues of SiC materials for future nuclear systems, Scr. Mater. 143 (2018) 149–153 https://doi.org/10.1016/j.

scriptamat.2017.03.001.
[4] X. Liu, Z. Yu, R. Ishikawa, L. Chen, X. Yin, Y. Ikuharad, R. Riedel, Single-source-precursor synthesis and electromagnetic properties of novel RGO-SiCN ceramic nanocomposites, J. Mater. Chem. C 5 (2017) 7950–7960 https://doi.org/10.1039/C7TC00395A.
[5] F. Dalcanale, J. Grossenbacher, G. Blugan, M.R. Gullo, A. Lauria, J. Brugger, H. Tevaearai, T. Graule, M. Niederberger, J. Kuebler, Influence of carbon enrichment on electrical conductivity and processing of polycarbosilane derived ceramic for MEMS applications, J. Eur. Ceram. Soc. 34 (2014) 3559–3570 https://doi.org/10.1016/j.jeurceramsoc.2014.06.002.
[6] T. Konegger, R. Patidar, R.K. Bordia, A novel processing approach for free-standing porous non-oxide ceramic supports from polycarbosilane and polysilazane precursors, J. Eur. Ceram. Soc. 35 (2015) 2679–2683 https://doi.org/10.1016/j.jeurceramsoc.2015.03.009.
[7] Z. Li, Y. Wang, L. An, Control of the thermal conductivity of SiC by modifying the polymer precursor, J. Eur. Ceram. Soc. 37 (2017) 61–67 https://doi.org/10.1016/j.jeurceramsoc.2016.08.023.
[8] Y.S. Jang, M. Jank, V. Maier, K. Durst, N. Travitzky, C. Zollfrank, SiC ceramic micropatterns from polycarbosilanes, J. Eur. Ceram. Soc. 30 (2010) 2773–2779 https://doi.org/10.1016/j.jeurceramsoc.2010.05.019.
[9] R. Yao, Z. Feng, Y. Yu, S. Li, L. Chen, Y. Zhang, Synthesis and characterization of continuous freestanding silicon carbide films with polycarbosilane (PCS), J. Eur. Ceram. Soc. 29 (2009) 2079–2085 https://doi.org/10.1016/j.jeurceramsoc.2008.11.019.
[10] P. Wang, L. Cheng, Y. Zhang, H. Wu, Y. Hou, W. Yuan, L. Zheng, Flexible, hydrophobic SiC ceramic nanofibers used as high frequency electromagnetic wave absorbers, Ceram. Int. 43 (2017) 7424–7435 https://doi.org/10.1016/j.ceramint.2017.03.001.
[11] P.H. Rodríguez, E.L. Honorato, Polymer derived SiC environmental barrier coatings with superwetting properties, Ceram. Int. 43 (2017) 11289–11295 https://doi.org/10.1016/j.ceramint.2017.05.326.
[12] X. Liu, L. Zhang, X. Yin, F. Ye, Y. Liu, L. Cheng, The microstructure and electromagnetic wave absorption properties of near-stoichiometric SiC fibre, Ceram. Int. 43 (2017) 3267–3273 https://doi.org/10.1016/j.ceramint.2016.11.158.
[13] R. Zhou, L. Liao, Z. Chen, L. Zhong, X. Xu, Y. Han, Y. Zhong, Y. Zheng, R. Yao, Fabrication of monolithic rGO/SiC(O) nanocomposite ceramics via precursor (polycarbosilane-vinyltriethoxysilane-graphene oxide) route, Ceram. Int. 44 (2018) 14929–14934 https://doi.org/10.1016/j.ceramint.2018.05.084.
[14] Y. Xia, R. Fang, Z. Xiao, L. Ruan, R. Yan, H. Huang, C. Liang, Y. Gan, J. Zhang, X. Tao, W. Zhang, Supercritical fluid assisted biotemplating synthesis of Si–O–C microspheres from microalgae for advanced Li-ion batteries, RSC Adv. 6 (2016) 69764–69772 https://doi.org/10.1039/c6ra13560a.
[15] M.A. Abass, A.A. Syed, C. Gervais, G. Singh, Synthesis and electrochemical performance of a polymer-derived silicon oxycarbide/boron nitride nanotube composite, RSC Adv. 7 (2017) 21576–21584 https://doi.org/10.1039/c7ra01545c.
[16] S. Kaur, R. Riedel, E. Ionescu, Pressureless fabrication of dense monolithic SiC ceramics from a polycarbosilane, J. Eur. Ceram. Soc. 34 (2014) 3571–3578 https://doi.org/10.1016/j.jeurceramsoc.2014.05.002.
[17] V. Proust, M.C. Bechelany, R. Ghisleni, M. Beaufort, P. Miele, S. Bernard, Polymer-derived Si-C-Ti systems: from titaniμm nanoparticle-filled polycarbosilanes to dense monolithic multi-phase components with high hardness, J. Eur. Ceram. Soc. 36 (2016) 3671–3679 https://doi.org/10.1016/j.jeurceramsoc.2016.04.023.
[18] H. Chen, X. Wang, F. Xue, Y. Huang, K. Zhou, D. Zhang, 3D printing of SiC ceramic: direct ink writing with a solution of preceramic polymers, J. Eur. Ceram. Soc. 38 (2018) 5294–5300 https://doi.org/10.1016/j.jeurceramsoc.2018.08.009.
[19] M. Yu, O.T. Picot, T.G. Saunders, I. Dlouhý, J. Feng, M.M. Titirici, A. Mahajan, M.J. Reece, Graphene-reinforced silicon oxycarbide composites prepared by phase transfer, Carbon 139 (2018) 813–823 https://doi.org/10.1016/j.carbon.2018.07.042.
[20] M.A. Mazo, A. Tamayo, A.C. Caballero, J. Rubio, Enhanced electrical and thermal conductivities of silicon oxycarbide nanocomposites containing carbon nanofibers, Carbon 138 (2018) 42–51 https://doi.org/10.1016/j.carbon.2018.05.075.
[21] R. Riedel, L. Toma, E. Janssen, J. Nuffer, T. Melz, H. Hanselka, Piezoresistive effect in SiOC ceramics intergrated pressure sensors, J. Am. Ceram. Soc. 93 (2010) 920–924 https://doi.org/10.1111/j.1551-2916.2009.03496.x.
[22] R. Riedel, G. Mera, R. Hauser, A. Klonczynski, Silicon-based polymer-derived ceramics: synthesis properties and applications-A review, J. Ceram. Soc. Jpn. 114 (2006) 425–444 https://doi.org/10.2109/jcersj.114.425.
[23] N. Liao, B. Zheng, H. Zhou, W. Xue, Effect of carbon content on the structure and electronic properties of silicon oxycarbide anodes for lithiumion batteries: a first-principles study, J. Mater. Chem. A 3 (2015) 5067–5071 https://doi.org/10.1039/c4ta06932c.
[24] L. Duan, Q. Ma, L. Mei, Z. Chen, Fabrication and electrochemical performance of nanoporous carbon derived from silicon oxycarbide, Microporous Mesoporous Mater. 202 (2015) 97–105 https://doi.org/10.1016/j.micromeso.2014.09.047.
[25] K. Lu, D. Erb, M. Liu, Thermal stability and electrical conductivity of carbon-enriched silicon oxycarbide, J. Mater. Chem. C 4 (2016) 1829–1837 https://doi.org/10.1039/c6tc00069j.
[26] G.M. Renlund, S. Prochazka, R.H. Doremus, Silicon oxycarbide glasses: Part II. Structure and properties, J. Mater. Res. 6 (1991) 2723–2734 https://doi.org/10.1557/JMR.1991.2723.
[27] J. Kaspar, M.G. Zajac, S. Choudhury, R. Riedel, Impact of the electrical conductivity on the lithium capacity of polymer-derived silicon oxycarbide (SiOC) ceramics, Electrochim. Acta 216 (2016) 196–202 https://doi.org/10.1016/j.electacta.2016.08.121.
[28] K.J. Kim, J.H. Eom, T.J. Koh, Y.W. Kim, W.S. Seo, Effects of carbon addition on the electrical properties of bulk silicon-oxycarbide ceramics, J. Eur. Ceram. Soc. 36 (2016) 2705–2711 https://doi.org/10.1016/j.jeurceramsoc.2016.04.034.
[29] G. Prakash, M.A. Capano, M.L. Bolen, D. Zemlyanov, R.G. Reifenberger, AFM study of ridges in few-layer epitaxial graphene grown on the carbon-face of 4H-SiC(0001), Carbon 48 (2010) 2383–2393 https://doi.org/10.1016/j.carbon.2010.02.026.
[30] B. Román-Manso, F.M. Figueiredo, B. Achiaga, R. Barea, D. Pérez-Coll, A.M. Gómez, M. Terrones, M.I. Osendi, M. Belmonte, P. Miranzo, Electrically functional 3D-architectured graphene/SiC composites, Carbon 100 (2016) 318–328 https://doi.org/10.1016/j.carbon.2015.12.103.
[31] R. Sujith, P.K. Chauhan, J. Gangadhar, A. Maheshwari, Graphene nanoplatelets as nanofillers in mesoporous silicon oxycarbide polymer derived ceramics, Sci. Rep-UK 8 (2018) 17633 https://doi.org/10.1038/s41598-018-36080-1.
[32] Y. Chen, X. Yang, Y. Cao, Z. Gan, L. An, Quantitative study on structural evolutions and associated energetics in polysilazane-derived amorphous silicon carbonitride ceramics, Acta Mater. 72 (2014) 22–31 https://doi.org/10.1016/j.actamat.2014.03.049.
[33] V.S. Pradeep, M. Graczyk-Zajac, M. Wilamowska, R. Riedel, G.D. Soraru, Influence of pyrolysis atmosphere on the lithium storage properties of carbon-rich polymer derived SiOC ceramic anodes, Solid State Ion. 262 (2014) 22–24 https://doi.org/10.1016/j.ssi.2013.08.043.
[34] O. Tapasztó, V. Puchy, Z.E. Horváth, Z. Fogarassy, E. Bódis, Z. Károly, K. Balázsia, J. Duszab, L. Tapasztó, The effect of graphene nanoplatelet thickness on the fracture toughness of Si_3N_4 composites, Ceram. Int. 45 (2019) 6858–6862 https://doi.org/10.1016/j.ceramint.2018.12.180.
[35] Z. Dong, J. Meng, H. Zhu, G. Yuan, Y. Cong, J. Zhang, X. Li, A. Westwood, Synthesis of SiC nanowires via catalyst-free pyrolysis of silicon-containing carbon materials derived from a hybrid precursor, Ceram. Int. 43 (2017) 11006–11014 https://doi.org/10.1016/j.ceramint.2017.05.142.
[36] K. Lu, J. Li, Fundamental understanding of water vapor effect on SiOC evolution during pyrolysis, J. Eur. Ceram. Soc. 36 (2016) 411–422 https://doi.org/10.1016/j.jeurceramsoc.2015.11.003.
[37] Y. Lin, Y. Lu, Y. Gao, Y. Chen, Z. Chen, Measuring the thermal resistance of LED packages in practical circumstances, Thermochim. Acta 520 (2011) 105–109 https://doi.org/10.1016/j.jeurceramsoc.2018.07.010.
[38] Y. Tang, S. Qiu, M. Li, K. Zhao, Fabrication of alumina/copper heat dissipation substrates by freeze tape casting and melt infiltration for high-power LED, J. Alloy. Comp. 690 (2017) 469–477 https://doi.org/10.1016/j.tca.2011.03.026.
[39] S.-Y. Kwak, S.C. Yang, N.R. Kim, J.H. Kim, B.-S. Bae, Thermally stable, dye-bridged nanohybrid-based white light-emitting diodes, Adv. Mater. 23 (2011) 5767–5772 https://doi.org/10.1016/j.jallcom.2016.08.149.
[40] R. Ma, D. Erb, K. Lu, Flash pyrolysis of polymer-derived SiOC ceramics, J. Eur. Ceram. Soc. 38 (2018) 4906–4914 https://doi.org/10.1002/adma.201103077.